R. Riva, M. Spinelli, L. Sartori, S. Cacciola, A. Croce
Stability Analysis of Wind Turbines with Bend-Twist Coupled Blades
Journal of Physics: Conference Series, Vol. 1037, 2018, 062014 (10 pages)
doi:10.1088/1742-6596/1037/6/062014

Stability analysis of wind turbines with bend-twist coupled blades

IOP Conf. Series: Journal of Physics: Conf. Series **1037** (2018) 062014 doi:10.1088/1742-6596/1037/6/062014

Stability analysis of wind turbines with bend-twist coupled blades

R Riva[1,2], M Spinelli[2], L Sartori[2], S Cacciola[2], A Croce[2]

[1] Wind Energy Department, Technical University of Denmark, Frederiksborgvej 399, DK-4000 Roskilde, Denmark

[2] Dipartimento di Scienze e Tecnologie Aerospaziali, Politecnico di Milano, Via La Masa 34, 20156 Milano, Italy.

E-mail: ricriv@dtu.dk, marco6.spinelli@mail.polimi.it, {luca.sartori, stefano.cacciola, alessandro.croce}@polimi.it

Abstract. Over the last years, bend-twist coupling (BTC) has become one of the most important passive load reduction techniques in wind turbine blades. The kind and amount of BTC is often decided on the basis of the load reduction, often forgetting the related stability implications. In this work we perform the stability analysis of a very large wind turbine, where the BTC is obtained by rotating the fibers of the spar caps. The study focuses first on the isolated blade, and then on the complete wind turbine. The findings show that this BTC leaves some modes unaffected, but reduces the damping of the collective edgewise mode.

1. Introduction

Designing wind turbines with cyclic load reduction capabilities is one of the major concerns when it comes to developing very large and flexible rotors. This goal can be obtained with both active and passive solutions. Active control systems, e.g. individual pitch control, can substantially reduce loads but may necessitate additional sensors and increase the actuator duty cycle. On the other hand, passive control systems do not suffer from these drawbacks. A widespread passive control system is the bend-twist coupling (BTC) [1], which can be realized in many ways. A classical solution is to exploit the anisotropic nature of the composite materials used for manufacturing wind turbine blades. It is possible to rotate the fibers of the skin, or of the spar caps, away from the pitch axis, to get a bend-twist-to-feather coupling. In this way, a flapwise deflection corresponds to a reduction in the angle of attack, that in turn reduces the flapwise load. Alternative solutions may be obtained by applying an offset to the spar caps [2], or by backward sweeping the blades [3].

The effects of BTC are typically evaluated in terms of load alleviation and fatigue, but little has been done to investigate its impact on the overall turbine stability. Assessing the effects of BTC also from the stability standpoint results to be essential when very large turbines are of interest, considering that they may be prone to vibrations associated by low damped modes [4]. In Refs. [5, 6], Stäblein *et al.* considered the DTU 10 MW reference wind turbine, and added off-diagonal terms to the stiffness matrix of its blades, this way obtaining generic bend-twist couplings. They evaluated the stability of a blade section, of the isolated blade, and finally of the complete wind turbine.

In this work, we want to study the stability of a particular type of BTC, realized by rotating the fibers of the spar caps. To this end, we have selected two versions of the AVATAR wind turbine, with and without BTC [7, 8, 9]. The analysis focused first on the isolated blade, and then on the complete wind turbine operating in normal wind profile conditions.

The stability analysis is conducted through an identification based approach, which has the advantage of being model independent and, hence, able to easily cope with the complexity that characterizes modern high-fidelity simulation tools, employed for wind turbine aero-servo-elastic analysis [10].

The paper is organized according to the following plan. In Sec. 2 the stability algorithms are illustrated. Afterward, in Sec. 3 the results of such analysis are reported for different applications of interest. Finally, Sec. 4 concludes the paper by summarizing the main findings.

2. Methodology

When a wind turbine is subject to a steady wind, its degrees of freedom undergo a periodic motion. Linearizing a model over this trajectory produces a linear time-periodic system, that the Coleman transformation converts into a time-invariant one only if the rotor is isotropic. Three-bladed wind turbines are perfectly isotropic if the blades are identical, the inflow uniform and in absence of gravity. Therefore, wind turbine models will be always characterized by a certain level of anisotropy in realistic conditions, and their stability has to be evaluated within a periodic framework, i.e. by using Floquet theory [10, 11].

In Ref. [10], a periodic auto-regressive with exogenous input (PARX) model is identified from suitable input/output series recorded from a virtual model of a multi-MW wind turbine in steady winds. The stability of the resulting model is then evaluated with the discrete-time Floquet theory. In the next, we will briefly explain the PARX algorithm and the subsequent stability analysis.

2.1. Identification algorithm

The identification of the PARX model can be performed through the prediction error methods (PEM), i.e. by minimizing a cost function depending on the difference between the measured and the predicted output. Two different approaches can be followed, the equation-error and the output-error.

In the equation-error framework, the measured output $y(k)$, being k the discrete time index, is assumed to be generated by the following process,

$$y(k) = \sum_{i=1}^{N_a} a_i(k-i)y(k-i) + \sum_{j=0}^{N_b} b_j(k-j)u(k-j) + e(k). \tag{1}$$

where, $u(k)$ is the input, N_a the number of delays in the auto-regressive part, and N_b the number of delays of the exogenous one. The parameters $a_i(k)$ and $b_j(k)$ are assumed to be periodic, with period K. Finally, $e(k)$ is a noise, with zero-mean and periodic variance. It is possible to prove that the optimal predictor associated to process (1) is

$$\hat{y}(k) = \sum_{i=1}^{N_a} a_i(k-i)y(k-i) + \sum_{j=0}^{N_b} b_j(k-j)u(k-j), \tag{2}$$

where $\hat{y}(k)$ indicates the predicted output. To reduce the number of parameters to be identified,

$a_i(k)$ and $b_j(k)$ are approximated by truncated Fourier series

$$a_i(k) = a_{i_0} + \sum_{l=1}^{N_{F_a}} \left(a_{i_l}^c \cos(l\varphi(k)) + a_{i_l}^s \sin(l\varphi(k)) \right), \tag{3a}$$

$$b_j(k) = b_{j_0} + \sum_{m=1}^{N_{F_b}} \left(b_{j_m}^c \cos(m\varphi(k)) + b_{j_m}^s \sin(m\varphi(k)) \right), \tag{3b}$$

with N_{F_a} the number of harmonics in the autoregressive part, N_{F_b} the number of harmonics in the exogenous one, and $\varphi(k)$ the rotor azimuth. The harmonics of these series constitute the parameters to be estimated, which are collected in the array $\boldsymbol{p} = (\dots, a_{i_0}, a_{i_l}^c, a_{i_l}^s, \dots, b_{j_0}, b_{j_m}^c, b_{j_m}^s, \dots)^\mathsf{T}$. This array is estimated by minimizing the following cost function

$$J = \frac{1}{N} \sum_{k=N_s}^{N} (y(k) - \hat{y}(k; \boldsymbol{p}))^2, \tag{4}$$

with $N_s = \max(N_a, N_b)$ and N the time index of the last measured output. Since the predicted output is linear in the parameters, the minimization of J is obtained by solving a least-squares problem.

In the output-error process, a "noise-free" output $\tilde{y}(k)$ is assumed to follow by a PARX sequence as

$$\tilde{y}(k) = \sum_{i=1}^{N_a} a_i(k-i)\tilde{y}(k-i) + \sum_{j=0}^{N_b} b_j(k-j)u(k-j), \tag{5}$$

while the measured output is instead corrupted by a zero-mean white noise with periodic variance

$$y(k) = \tilde{y}(k) + e(k). \tag{6}$$

It can be proved that the optimal predictor associated to process (6) is

$$\hat{y}(k) = \sum_{i=1}^{N_a} a_i(k-i)\hat{y}(k-i) + \sum_{j=0}^{N_b} b_j(k-j)u(k-j). \tag{7}$$

The parameters are again estimated by minimizing the cost function (4), this time using the predictor (7). Since the output-error predictor is nonlinear in the parameters, the minimization involves an iterative process, initialized by the guess provided by the equation-error.

2.2. Floquet theory in discrete-time

In Ref. [10] it is shown that the output-error process (6) is equivalent to (i.e. it has the same impulse response of) the following periodic system in the state-space form,

$$\boldsymbol{x}(k+1) = \boldsymbol{A}(k)\boldsymbol{x}(k) + \boldsymbol{B}(k)u(k), \qquad \boldsymbol{x}(0) = \boldsymbol{x}_0, \tag{8a}$$

$$y(k) = \boldsymbol{C}(k)\boldsymbol{x}(k) + D(k)u(k) + e(k), \tag{8b}$$

where

$$\left[\begin{array}{c|c} \boldsymbol{A}(k) & \boldsymbol{B}(k) \\ \hline \boldsymbol{C}(k) & D(k) \end{array}\right] = \left[\begin{array}{ccccc|c} 0 & 0 & \cdots & 0 & a_{N_s}(k) & b_{N_s}(k) + a_{N_s}(k)b_0(k) \\ 1 & 0 & \cdots & 0 & a_{N_s-1}(k) & b_{N_s-1}(k) + a_{N_s-1}(k)b_0(k) \\ 0 & 1 & \cdots & 0 & a_{N_s-2}(k) & b_{N_s-2}(k) + a_{N_s-2}(k)b_0(k) \\ \vdots & \ddots & \ddots & \vdots & \vdots & \vdots \\ 0 & 0 & \cdots & 1 & a_1(k) & b_1(k) + a_1(k)b_0(k) \\ \hline 0 & 0 & \cdots & 0 & 1 & b_0(k) \end{array}\right]. \tag{9}$$

The stability analysis of this system is performed by applying Floquet theory, as shown in Ref. [10], which we briefly review in the remaining part of this section.

The motion of $\boldsymbol{x}(k)$, and hence the stability of the system, is governed by the state transition matrix $\boldsymbol{\Phi}(k,\kappa)$ which evolves according to

$$\boldsymbol{\Phi}(k+1,\kappa) = \boldsymbol{A}(k)\boldsymbol{\Phi}(k,\kappa), \qquad \boldsymbol{\Phi}(\kappa,\kappa) = \boldsymbol{I}, \tag{10}$$

with $\boldsymbol{I}$ the identity matrix. By sampling the state at every period, we can see that its motion is governed by the monodromy matrix $\boldsymbol{\Psi}_\kappa = \boldsymbol{\Phi}(\kappa+K,\kappa)$. The eigenvalues θ_j of $\boldsymbol{\Psi}_\kappa$ are termed characteristic multipliers, and the system is asymptotically stable if they lie within the open unit disk, i.e. if

$$|\theta_j| < 1, \qquad \forall j \in [1,\dots,N_s]. \tag{11}$$

The free response of system (8) can be computed as

$$y(k) = \boldsymbol{C}(k)\boldsymbol{\Phi}(k,\kappa)\boldsymbol{x}(\kappa), \tag{12}$$

where $\boldsymbol{C}(k)\boldsymbol{\Phi}(k,\kappa)$ is named observed state transition matrix. It can be proved that the modal decomposition of this matrix is given by

$$\boldsymbol{C}(k)\boldsymbol{\Phi}(k,\kappa) = \sum_{j=1}^{N_s}\sum_{n=0}^{K-1} \psi_{j_n}\boldsymbol{\varrho}_j^{\mathsf{T}}(\kappa)\,(\eta_{j_n})^{k-\kappa}\,e^{\imath n\frac{2\pi}{K}\kappa}, \tag{13}$$

with

$$\eta_{j_n} = \sqrt[K]{|\theta_j|}\exp\left(\imath\frac{\angle(\theta_j)+2n\pi}{K}\right) \tag{14}$$

and $\imath = \sqrt{-1}$. The modal decomposition shows that each mode j is characterized by K harmonics, composed by the characteristic exponents η_{j_n}, and by the associated observed periodic mode shapes ψ_{j_n}. To assess the relative importance of each harmonic within a specified mode, we introduce the output-specific participation factor

$$\phi_{j_n} = \frac{|\psi_{j_n}|}{\sum_n |\psi_{j_n}|}. \tag{15}$$

When selecting as reference frame the multi-blade coordinates, the harmonic with the highest ϕ_{j_n} is labeled principal. The characteristic exponents play the same role of the eigenvalues of a linear time-invariant system, and can be converted in continuous time with

$$\eta_{j_n}^{\text{cont.}} = \frac{1}{\Delta t}\ln(\eta_{j_n}) \tag{16}$$

where Δt is the time step. The natural frequencies f_{j_n} and damping ratios ξ_{j_n} are then obtained as

$$f_{j_n} = \frac{|\eta_{j_n}^{\text{cont.}}|}{2\pi}, \qquad \xi_{j_n} = -\frac{\text{Re}(\eta_{j_n}^{\text{cont.}})}{|\eta_{j_n}^{\text{cont.}}|}. \tag{17}$$

3. Applications

3.1. Description of the system

As part of this study, we have designed two different structural configurations of the AVATAR blade. Both are based on the common *spar-box* internal arrangement depicted in Fig. 1. According to the AVATAR specifications, both the suction-side and the pressure-side spar caps are manufactured from plies of high-modulus unidirectional carbon fiber. The mechanical properties of the materials

are given in [12], together with an account of the primary design assumptions. One of the blades, hereafter called AVATAR vers4 was designed within a classic approach, that is, no extra-diagonal couplings were introduced in its structure. On the contrary, a second blade AVATAR vers4 BTC was equipped with a certain amount of fiber rotation, namely 5 degrees, in the two spar caps to achieve the desired bend-twist coupling mechanism.

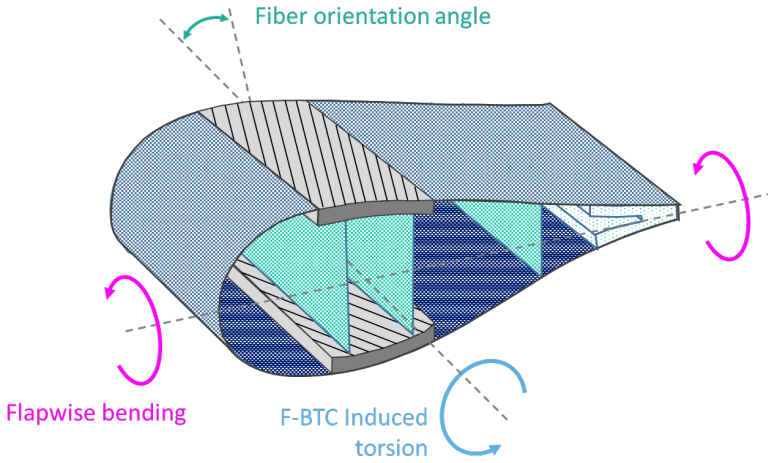

Figure 1: Spar-box sectional arrangement with BTC.

This is a common approach to generate a bend-twist coupled behavior already analyzed in previous investigations on the subject, see [6] and references therein. However, most studies do not recur to a complete redesign of the BTC blade, as they typically apply a certain level of coupling to the fibers without redesigning the structure. Obviously, this strategy can be helpful when a pure evaluation of the effects of BTC is sought, e.g. the actual load alleviation for a given structural layout. However, in our opinion, a complete understanding of the structural tailoring must account for the variations of the structure which are a direct consequence of the load alleviation mechanism. The best way to ensure the consistency, naturally, is to redesign the structure of the blade *after* the introduction of BTC. To gain a precise insight, then, we performed a mass-minimizing structural optimization of both configurations with our multi-disciplinary design algorithm `Cp-Max`. The details of the formulation are provided to the interested reader by Bottasso et al. [13]. This way, both structures are obtained from the same procedure and are truly comparable against each other. It must be noticed that one of the known drawbacks of the induced torsion associated to the BTC is a slight reduction of the energy production, as the larger torsional deformations move the airfoils away from their optimal points. To compensate this loss, we re-tuned the control system of the coupled solution by reducing the collective fine pitch in the partial-loading region of the power curve. A complete description of the procedure has been given in Ref. [9] as part of AVATAR dissemination activities.

It must be noticed that the design of the two wind turbines is based on the aero-servo-elastic simulator `Cp-Lambda` [14], which provides a multi-body modeling of the entire wind turbine and the possibility to compute the time-histories of the required loads and deformations. Within this formulation, the beam model used for blades and tower is geometrically exact, with a fully populated stiffness matrix, so as to correctly capture all the complex BTC blade behavior. The aerodynamics is rendered through the classical blade-element momentum theory, with the quasi-steady approximation, and includes the tower shadow.

3.2. Stability analysis of the isolated blade

In the course of the AVATAR project, it has been observed multiple times that the design load cases DLCs 6.2 (storm wind conditions, with rotor parked or idling) may cause the wind turbine to become unstable. Since the turbulent wind complicates the analysis, we have preferred to study a simplified problem, as proposed in Ref. [4] by Stettner *et al.* In this subsection, the blade is clamped at the root, with an arbitrary pitch angle.

The two versions of the AVATAR blade are first analyzed in vacuo. Table 1 lists the structural frequencies obtained by `Cp-Lambda`, without structural damping. As we can see, the BTC has

Table 1: First structural frequencies of the AVATAR blades.

#	AVATAR vers4 [Hz]	AVATAR vers4 BTC [Hz]	Name
1	0.643	0.611	1^{st} Flap
2	0.755	0.745	1^{st} Edge
3	1.823	1.741	2^{nd} Flap
4	2.246	2.181	2^{nd} Edge
5	3.719	3.553	3^{rd} Flap
6	4.794	4.645	3^{rd} Edge
7	6.140	5.891	4^{th} Flap
8	6.807	7.075	1^{st} Torsion
9	8.288	8.109	4^{th} Edge
10	9.079	8.764	5^{th} Flap

caused a reduction of all the frequencies, with the sole exception of the torsional one, which is increased. This is not surprising, as the rotation of the carbon fibers increases the torsional stiffness to the detriment of the flapwise bending one.

As done in Ref. [4] we have proceeded by applying a steady wind, having a magnitude of 42 m/s. In our model the pitch angle follows the usual convention, i.e. 90 deg indicates the full feather position. Once again, the structural damping is excluded, so as to measure only the aerodynamic damping. Since the analyses were conducted for the isolated blade, the estimation of frequencies and damping factors has been performed through the ARX algorithm as described in Sec. 2.1, without considering the periodic part. To perform the identification we have applied a zero-mean impulse at the tip in the edgewise direction, tuned so as to excite the first edgewise mode. As output channel, we have selected the edgewise bending moment at the root. Since the wind is constant, we have set $N_b = 1$, while with a trial and error approach we have set $N_a = 20$. Fig. 2 shows the identified damping ratio of the first edgewise mode. When the angle of attack lies in a region of negative $C_L - \alpha$ slope, the damping ratio becomes negative, a phenomenon known as stall-induced vibrations [15]. This BTC has a negligible effect on the stall-induced vibrations, but slightly diminishes the damping between -60 and $+80$ deg. This observation confirms that the stall-induced vibrations can be viewed as if they were induced by mild instabilities, Ref. [15].

At this point, a sensitivity analysis of the damping factors with respect to the structural damping was performed. In `Cp-Lambda` the structural damping is modeled with dissipative forces $\boldsymbol{f}(\eta)$ and moments $\boldsymbol{m}(\eta)$, distributed along the span η. These terms are proportional to the stiffness matrix $\boldsymbol{K}(\eta)$ and the strain rate $\dot{\boldsymbol{\epsilon}}(\eta)$, according to

$$\begin{pmatrix} \boldsymbol{f}(\eta) \\ \boldsymbol{m}(\eta) \end{pmatrix} = \mu(\eta)\boldsymbol{K}(\eta)\dot{\boldsymbol{\epsilon}}(\eta), \tag{18}$$

with $\mu(\eta)$ the structural damping coefficient. We have gradually increased the structural damping of the bend-twist coupled blade, keeping $\mu(\eta)$ uniform over the span, and identified the first

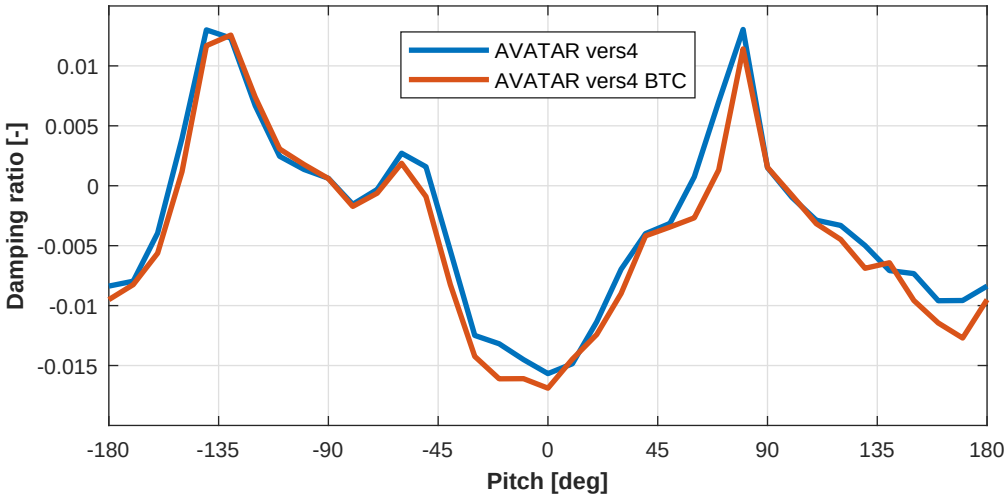

Figure 2: Damping ratio of the first edgewise mode.

modes. The result is visible in Fig. 3, which shows the relationship between the structural and the modal damping. The behavior is pretty linear with small deviations, typically related to mild

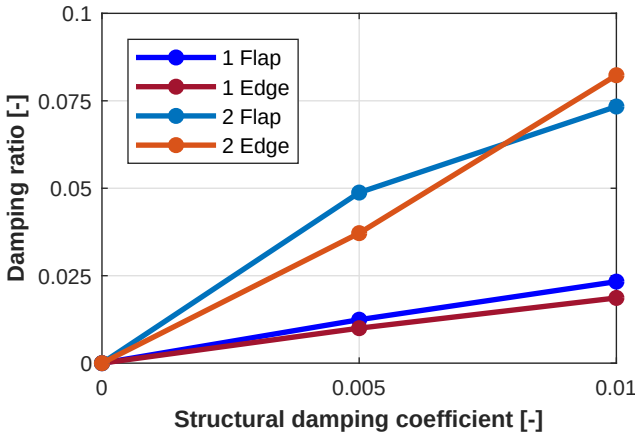

Figure 3: Modal damping ratio of the first modes of the isolated blade, as a function of the structural damping coefficient.

intrinsic errors in the identification process. Fig. 3 shows that the enhancement of structural damping, obtained by carefully designing the blades and choosing the material, may mitigate the stall-induced vibrations, as previously noted in Ref. [15].

3.3. Stability analysis of the complete wind turbine

Next, we have performed the stability analysis of the complete wind turbines by applying winds having a normal profile, from the cut-in till the cut-out speeds. The analysis concentrated on the first low-damped modes of the system.

To excite the tower side-side and the edgewise whirling modes, we have applied a zero-mean force impulse to the tower top, in the side-side direction, whereas for the edgewise collective mode, we have applied a torque doublet to the shaft. The blade root bending moments, recorded after the application of the perturbation, were Coleman-transformed and used as measurements

for the identification. Tower side-side and edgewise whirling modes are visible in the direct and quadrature axes, instead, the edgewise collective is observed in the average bending moment.

Finally, to excite the tower fore-aft mode an impulsive force in the fore-aft direction have been used and tower root fore-aft bending moment used as output measurements

Table 2 lists the most relevant harmonics that are observed in the rotating and fixed frames, i.e. on the blades and tower [15].

Table 2: Most relevant harmonics observed in the fixed, multiblade and rotating frames.

Mode	Fixed and multi-blade	Rotating
Tower	principal	$\pm\Omega$
Backward whirl	principal	$+\Omega$
Forward whirl	principal	$-\Omega$
Collective	principal	principal

The periodic Campbell diagram (see Ref. [10]) of the AVATAR wind turbine, with and without BTC, is shown in Fig. 4. As we can see, the tower side-side and the edgewise whirling modes result unmodified. On the other hand, the BTC has lowered both the frequency and damping of the edgewise collective mode. This might indicate that the BTC has diminished the flapwise component of the associated mode shape. The BTC has also lowered the damping ratio of the tower fore-aft, from about 17% to 15% for the principal harmonic. This reduction is due to the flapwise unloading generated by the BTC.

Finally, to investigate the effect of different control settings on the damping of the edgewise collective mode, we have performed a dedicated study, in which the minimum pitch angle of the AVATAR vers4 with BTC is set to 0 deg, which is the original minimum pitch angle. The result, displayed in Fig. 5, shows that decreasing the pitch angle in the partial power region makes the edgewise collective mode more stable.

4. Conclusions and future outlooks

In this work, we have conducted the stability analysis of the AVATAR wind turbine, with bend-twist coupled blades. By resorting to a system identification approach we have been able to assess the stability of the first low-damped modes of the system. For the results shown in this work, the following conclusions can be derived.

- The BTC has a minor effect on the response of the isolated blade in the case it is dominated by stall-induced vibrations.
- Dealing with the complete wind turbine, the edgewise whirling modes and the tower side-side mode characteristics are not affected by this BTC.
- On the contrary, BTC may reduce significantly the damping of the tower fore-aft and the edgewise collective modes.

In terms of possible extensions, the same approach may consider different types of BTC, like for example the one obtained by a spar caps displacing, in order to compare different BTC techniques from the stability standpoint. Further investigations should be devoted also to the evaluation of the effects of unsteady aerodynamics, on the stability characteristics of the rotor with and without BTC.

Acknowledgments

This work has been partially supported by the AVATAR project, which received funding from the European Union's Seventh Programme for research, technological development and demonstration under grant agreement No FP7-ENERGY-2013-1/no. 608396.

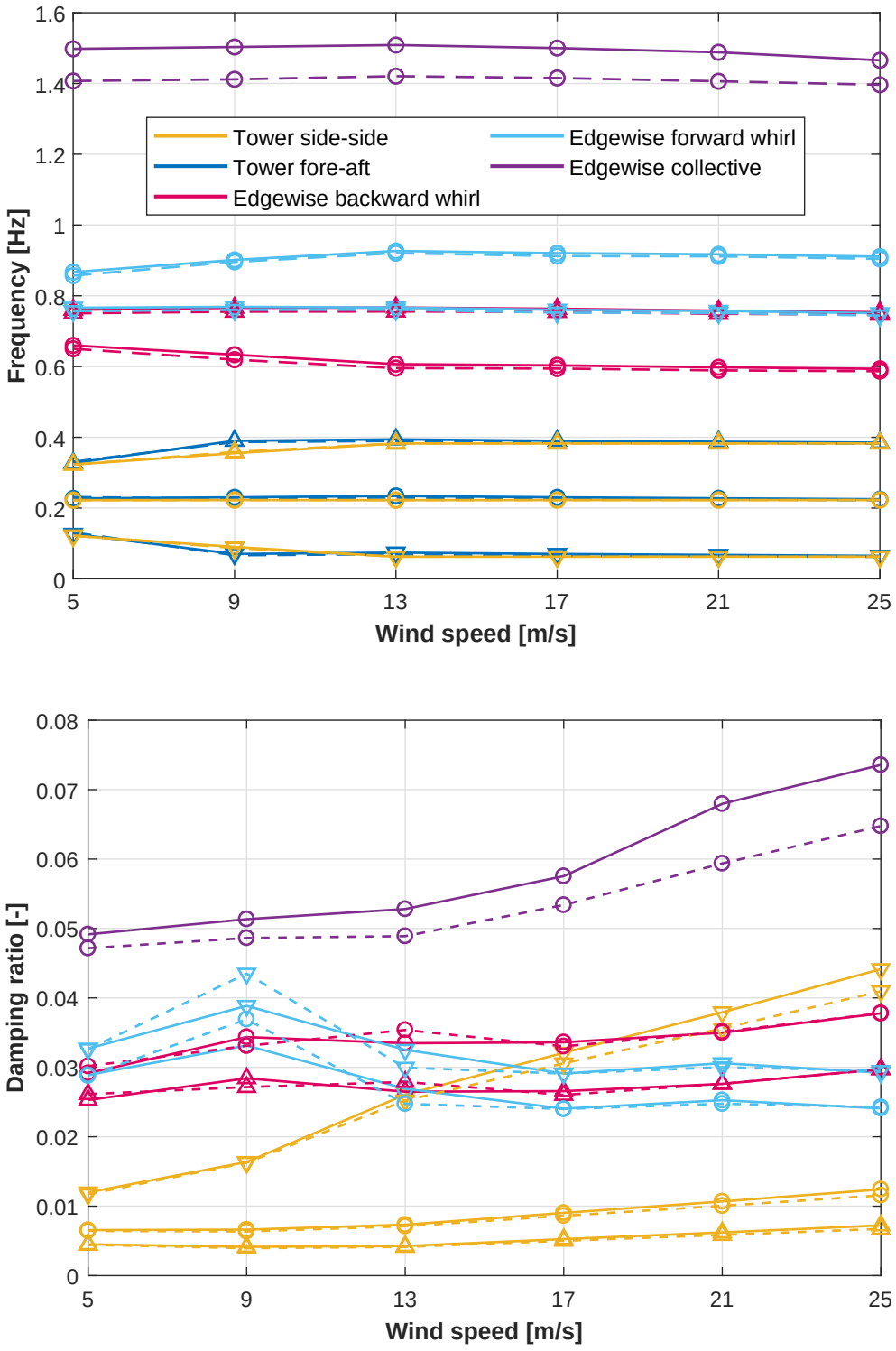

Figure 4: Periodic Campbell diagram of AVATAR vers4 (—) and AVATAR vers4 BTC (- - -). ○ indicates the principal harmonic, △ the $+\Omega$ harmonic and ▽ the $-\Omega$ harmonic. For clarity the damping ratio of the tower fore-aft mode is not shown.

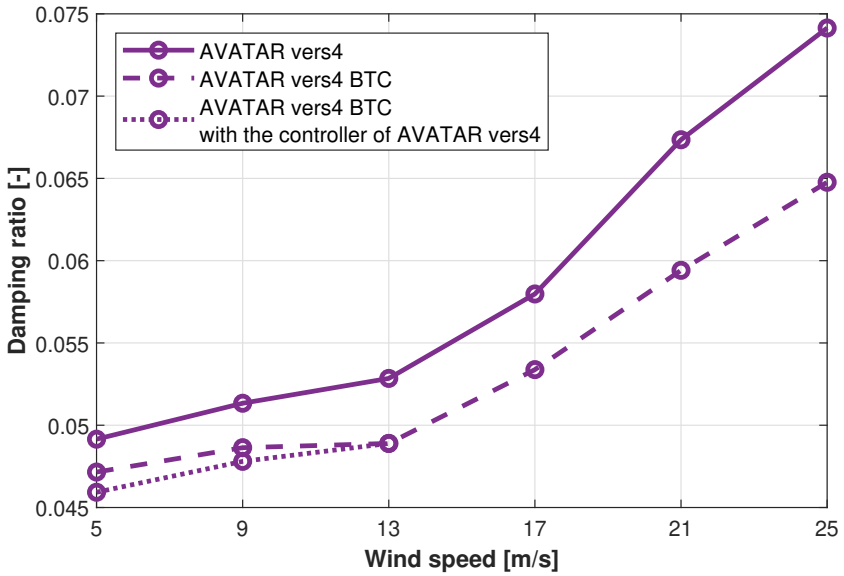

Figure 5: Damping ratio of the edgewise collective mode for three versions of the AVATAR wind turbine.

References

[1] Bottasso C L, Campagnolo F, Croce A and Tibaldi C 2012 Optimization-based study of bend-twist coupled rotor blades for passive and integrated passive/active load alleviation *Wind Energy* **16** 1149–66
[2] Croce A *et al.* Lightweight rotor design by optimal spar cap offset *J. Phys. Conf. Ser.* **753** 062003–10
[3] Hansen M H 2011 Aeroelastic properties of backward swept blades *49th AIAA Aerospace Sciences Meeting including the New Horizons Forum and Aerospace Exposition*
[4] Stettner M *et al.* 2016 Stall–Induced Vibrations of the AVATAR Rotor Blade *J. Phys. Conf. Ser.* **753** 042019
[5] Stäblein A R, Hansen M H, Pirrung G 2017 Fundamental aeroelastic properties of a bend-twist coupled blade section *J Fluid Struct* **68** 72–89
[6] Stäblein A R, Hansen M H and Verelst D R 2017 Modal properties and stability of bend-twist coupled wind turbine blades *Wind Energ. Sci.* **2** 343–60
[7] Schepers J G *et al.* 2015 AVATAR: AdVanced Aerodynamic Tools of lArge Rotors 33rd Wind Energy Symposium AIAA SciTech Forum
[8] Schepers J G *et al.* 2016 Latest results from the EU project AVATAR: Aerodynamic modelling of 10 MW wind turbines *J. Phys.: Conf. Ser.* **753** 022017
[9] Croce A *et al.* 2017 AVATAR Deliverable 4.12: Effect of blade flexibility and structural tailoring on loads
[10] Bottasso C L and Cacciola S 2015 Model-independent periodic stability analysis of wind turbines *Wind Energy* **18** 865–87
[11] Skjoldan P F and Hansen M H 2009 On the similarity of the Coleman and Lyapunov–Floquet transformations for modal analysis of bladed rotor structures *J. Sound. Vib.* **327** 424–439
[12] Lekou D *et al.* 2015 AVATAR Deliverable 1.2: Reference Blade Design
[13] Bottasso C L, Croce A and Campagnolo F 2012 Multi-disciplinary constrained optimization of wind turbines *Multibody System Dynamics* **27** 21-–53
[14] Bottasso C L and Croce A 2006 Cp-Lambda: user's manual *Dipartimento di Scienze e Tecnologie Aerospaziali, Politecnico di Milano*
[15] Hansen M H 2007 Aeroelastic instability problems for wind turbines *Wind Energy* **10**(6) 551–77